Journal of Hydrology 603 (2021) 126964

Contents lists available at ScienceDirect

Journal of Hydrology

journal homepage: www.elsevier.com/locate/jhydrol

Research papers

Exploring the utility of radar and satellite-sensed precipitation and their dynamic bias correction for integrated prediction of flood and landslide hazards

Sheng Wang [a,b], Ke Zhang [a,b,*], Lijun Chao [a], Donghuan Li [c], Xin Tian [d], Hongjun Bao [e], Guoding Chen [a], Yi Xia [a]

[a] State Key Laboratory of Hydrology-Water Resources and Hydraulic Engineering, and College of Hydrology and Water Resources, Hohai University, Nanjing, Jiangsu 210098, China
[b] Yangtze Institute for Conservation and Development, Hohai University, Nanjing 210098, China
[c] State Key Laboratory of Numerical Modeling for Atmospheric Sciences and Geophysical Fluid Dynamics, Institute of Atmospheric Physics, Chinese Academy of Sciences, Beijing 100029, China
[d] KWR Water Research Institute, Groningenhaven 7, 3433 PE Nieuwegein, The Netherlands
[e] National Meteorological Center, China Meteorological Administration, Beijing 100081, China

ARTICLE INFO

This manuscript was handled by Emmanouil Anagnostou, Editor-in-Chief, with the assistance of Pierre-Emmanuel Kirstetter, Associate Editor

ABSTRACT

It is important to develop the integrated flood and landslide modeling system driven by radar and satellite to predict these hazards to mitigate their damages. In this study, we investigated the utility of the C-band, one-polarization radar quantitative precipitation estimation (QPE) and the Global Satellite Mapping of Precipitation (GSMaP) satellite QPE for the integrated prediction of floods and landslides in two hilly basins of southern Shaanxi Province of China. We further developed a dynamic bias correction to reduce uncertainty in radar and satellite QPEs using gauge observations and explored the impacts of gauge density and spatial resolution of QPE on the effectiveness of bias correction. Our results show that the radar and GSMaP QPEs have respective large negative and positive biases. The bias-correction method has significantly improved the quality of both radar and GSMaP QPEs and the associated accuracies in the simulated hydrological processes and slope stability. The bias-correction method with a correction time interval of 24 h can achieve the optimal results for both radar and GSMaP QPEs. Although gauge density and spatial resolution impact the accuracy of the bias-corrected methods for both radar and GSMaP, inclusion of the observations from even a small number of rain gauges will be helpful for reducing the uncertainty in the radar and satellite QPEs.

1. Introduction

Rainfall-induced flood and landslide hazards are destructive and harmful to both of human lives and infrastructure (Blöthe et al., 2015; Huang et al., 2017; Peruccacci et al., 2012). Globally, economic losses caused by floods account for 30–40% of losses due to natural hazards during 1974–2003 (Guha-Sapir et al., 2004). With the rapid growth of population and economy, flood-induced losses are becoming more and more severe ()(Chen et al., 2021; He et al., 2018; Jonkman, 2005). Besides, landslides are responsible for more than 1000 deaths and approximately 4 billion US dollars in property losses per year (Pradhan and Youssef, 2010). China is also severely affected by natural hazards, including floods and landslides (Hong et al., 2015; Petley, 2010; Zhang et al., 2019b). The average property losses caused by flood are about 110 billion CNY per year while the death is more than 5000 in recent years. One study reports that landslide hazards have led to about 1100 fatalities and 5–10 billion US dollars since 2000 (Hong et al., 2017). Due to the massive fatalities and property losses caused by floods and landslides, it is essential to develop the forecasting capacity of these hazards to reduce and further avoid the damages (Chen et al., 2015).

Hydrological models for flood forecasting have developed from conceptual models (Burnash et al., 1973; Crawford and Linsley, 1966; Sugawara et al., 1984) to semi-distributed models (BEVEN and KIRKBY, 1979; Duan and Miller, 1997; Zhang et al., 2021) and further to fully

* Corresponding author at: State Key Laboratory of Hydrology-Water Resources and Hydraulic Engineering, and College of Hydrology and Water Resources, Hohai University, Nanjing, Jiangsu 210098, China.
E-mail address: kzhang@hhu.edu.cn (K. Zhang).

https://doi.org/10.1016/j.jhydrol.2021.126964
Received 21 March 2021; Received in revised form 24 July 2021; Accepted 13 September 2021
Available online 21 September 2021

distributed models. In the meantime, landslide prediction has evolved from heuristic susceptibility approaches (Fookes, 1997; Griffiths, 2002; Griffiths and Edwards, 2001; Guzzetti et al., 2000) to empirical rainfall threshold models (Bogaard and Greco, 2018; Caine, 1980; Glade et al., 2000; Guzzetti et al., 2007; Guzzetti et al., 2008) and further to physically-based slope stability models (Liao et al., 2010; Montrasio and Valentino, 2008; Montrasio and Valentino, 2016a; Montrasio and Valentino, 2016b; Van Asch et al., 2007; Wilkinson et al., 2002). Recently, coupling the hydrological models with slope stability models (He et al., 2016; Wang et al., 2020a; Zhang et al., 2016) have been developed to predict flood and landside simultaneously because the concept of cascading hazards has drawn more and more attention. Hydrological models can provide more accurate and realistic estimations of hydrological processes and states for slope stability model, *e.g.*, rainfall infiltration and soil moisture, which is proved to improve the predictive capability for the landslide hazards and extend the functionality of the hydrological models. Rainfall, as a key forcing data of hydrological models and landslide models, has a significant impact on flood forecasting and simulations of hydrological processes, and hence landslide prediction. Therefore, it is important to obtain rainfall data as accurate as possible.

Usually, rainfall data can be observed/estimated by ground gauge stations, weather radars, and meteorological satellites. Different rainfall data sources have their advantages and disadvantages for representing spatiotemporal characteristics of actual rainfall processes. Gauge rainfall is usually treated as the 'true' value of actual rainfall because it measures the rainfall that falls into the ground surface. However, gauge rainfall is a point-level observation and has to represent the rainfall spatial variability through a network, making its representation depending on station density and spatial distribution of stations. Moreover, distributed hydrological and land surface models require gridded rainfall as forcing, which requires interpolation of gauge rainfall, leading to some new errors and uncertainties (Hughes, 2006; Renard et al., 2010; Zhang et al., 2021). Radar rainfall can detect the spatial distribution of rainfall over a large region and often has a high temporal resolution, *e.g.*, 6 min. It is derived by constructing a quantitative relation between rainfall (*e.g.*, rainfall intensity) and reflectivity (Krajewski and Smith, 2002; Wilson and Brandes, 1979). Therefore, the accuracy of radar rainfall is directly influenced by the precipitation retrieval algorithms, which are usually built based on the distribution of raindrop size or rainfall rate (Atlas et al., 1990). In addition, the accuracy of radar rainfall is also affected by terrain and vegetation cover because they can occlude the electromagnetic waves emitted by radar (Qi and Zhang, 2013; Smith and Krajewski, 1991). The accuracy of radar rainfall may be low if the terrain is complex and vegetation is dense. Relative to radar, satellites can cover a much larger area (Hsu et al., 1997). Similar to radar rainfall, the relation between actual rainfall and reflectivity received by satellite is built through different retrieval algorithms (Griffith et al., 1978). So far, the common global satellite rainfall datasets include the Tropical Rainfall Measuring Mission (TRMM) (Kummerow et al., 1998), Global Satellite Mapping of Precipitation (GSMaP) of the Global Precipitation Measurement (GPM) mission (Ushio et al., 2003), Climate Prediction Center MORPHing (CMORPH) data (Joyce et al., 2004), the Integrated Multi-satellitE Retrievals for GPM (IMERG) (Huffman et al., 2019), and Precipitation Estimation from Remotely Sensed Information using Artificial Neural Networks (PERSIANN) (Hong et al., 2005) among others, which are based on different remote sensing sensors and retrieval algorithms. However, gauge-corrected satellite rainfall is often substantially time-lagged (Shen et al., 2010) while near real-time satellite rainfall has a low latency but a relatively high uncertainty. As a result, the above-mentioned limitations often limit the utility of satellite rainfall for, in particular, real-time flood forecasting of the small and medium-sized basins (Wu and Zhai, 2012). Gauge observations with automated quality control and reporting can overcome this shortcoming but it is usually unpractical to build dense gauge network for a large region. In addition, similar to near real-time satellite rainfall, gauge rainfall without automated quality control could be time-lagged if quality control need be conducted to correct the potential systematic errors.

Due to the biases in radar and satellite rainfall, it is important to develop bias-correction methods to improve the accuracy of radar and satellite rainfall data. In recent years, different bias-correction methods have been developed. For example, Cheema and Bastiaanssen (2012) adopted the regression analysis and geographical differential analysis (GDA) methods to calibrate the TRMM rainfall based on gauge rainfall data and found that the rainfall calibrated by the GDA method has a high accuracy. Chao et al. (2018) proposed a bias-correction method based on the mixed geographically weighted regression (MGWR) method for merging satellite and gauge rainfall, in which the weights were determined by four different weighting functions. The MGWR method improves the spatial resolution and quality of satellite rainfall and is valuable for hydrological modelling. Ma et al. (2018b) proposed a dynamic Bayesian Model Averaging (DBMA) scheme to blend multi-satellite precipitation products, providing a new solution for blending multi-satellite rainfall data. Although the applicability and evaluation of radar and satellite precipitation products for flood simulation and prediction have been widely studied recently, their applicability for landslide prediction and the prediction of rainfall-triggered multiple hazards such as floods and landslides have not been well studied. How to facilitate the integrated forecasting of flood and landslide hazards using the multi-source rainfall estimates and how to improve the forecasting accuracy by reducing the uncertainty in the multi-source rainfall estimates remain to be addressed.

Therefore, the objectives of this study are three-fold: (1) to investigate the utility of the C-band quantitative precipitation estimation (QPE) from a radar of China New Generation Weather Radar (CINRAD) network and the GSMaP satellite QPE of the GPM mission for integrated prediction of floods and landslides, (2) to develop a dynamic bias correction to reduce uncertainty in radar and satellite QPEs using gauge observations, and (3) to explore the impacts of gauge density and spatial resolution of QPE on the effectiveness of bias correction. To this end, we first compared the radar and satellite QPEs with the gauge observations and analyzed the uncertainties in these QPEs. We then developed a dynamic geographical differential analysis (DGDA) method to correct the biases in the QPEs. Finally, we conducted the hydrological evaluation of the original and bias-corrected QPEs and quantified the impacts of different rainfall sources on the integrated flood-landslide prediction/simulation via the integrated Coupled Routing and Excess storage and SLope-Infiltration-Distributed Equilibrium (iCRESLIDE v2.0) model (He et al., 2016; Wang et al., 2020b).

2. Study area and datasets

2.1. Study area

Our study area is located in the Shaanxi Province of northwest China (Fig. 1a), which frequently suffers from flood and landslide hazards. The statistical report shows that rainfall-induced landslide hazards occur frequently across Shaanxi, with more than 1,000 landslide events during 2009–2012, because of steep slopes in its many areas and heavy rainfall in the monsoon seasons (May to October) (Zhang et al., 2019a). Study area in this study is a nested region, with a bigger rectangular area shown in Fig. 1a and Fig. 1b ranging from 108°E to 110°E in longitude and from 31°N to 33°N in latitude and two basins (Fig. 1b) within the rectangular area. Within the rectangular area, we compared the gauge rainfall with the radar and satellite QPEs and analyzed the uncertainty in these QPEs. Within the basins, we conducted the iCRESLIDE simulations driven by the gauge observations and QPEs to conduct the hydrological evaluation of QPEs and evaluate the effectiveness of the dynamic bias correction method.

The two basins are located in southern Shaanxi and include the Ba River Basin and Lan River Basin (Fig. 1a). The Ba River Basin is a

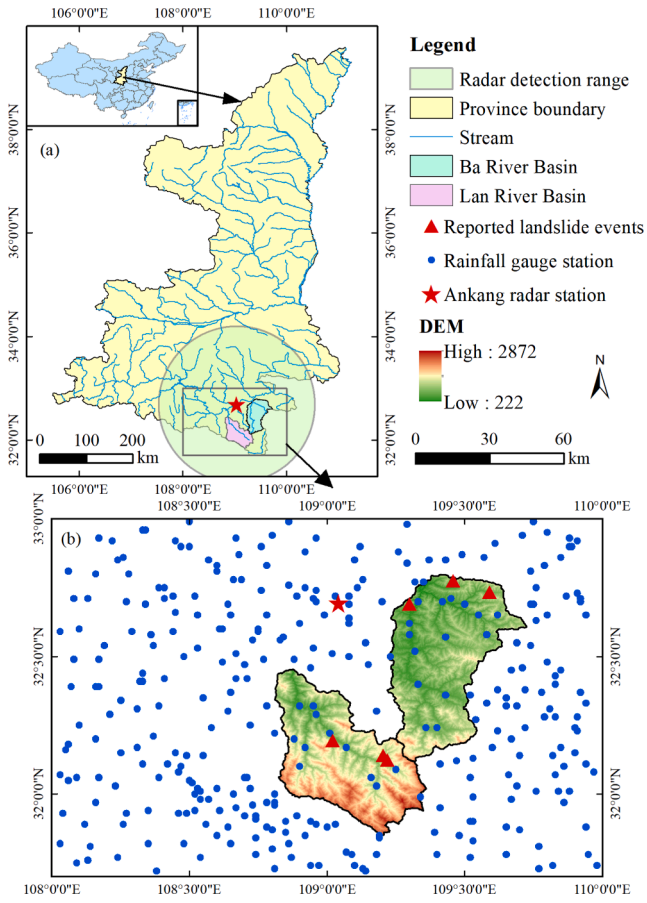

Fig. 1. (a) Locations of the study area and (b) distribution of the radar station, rainfall gauges, and recorded landslides used in this study.

tributary of the Han River, the largest tributary of the Yangzi River, and has an area of 2,069 km^2. Its elevation ranges from 222 to 2,473 m (Fig. 1b), and has an average slope of 22.8° (Fig. 2a). The average channel gradient of the Ba River is about 28.6 %. Annual rainfall in this basin is about 700–900 mm, of which summer (July to September) rainfall contributes for 40–60 %. Soil type is mainly loam in this basin (Fig. 2b), while forests cover most of its lands accompanied by a few cultivated lands in the plain area (Fig. 2c). The Lan River Basin is also a tributary of the Han River with an area of 1845 km^2. Elevation decreases from southeast to northwest, which is similar to that of the Ba River Basin (Fig. 1b). The average slope is 26.5° (Fig. 2d), which is steeper than that of the Ba River Basin. The Lan River often experiences flash floods and has the recorded highest peak flood of 2,220 m^3/s. The spatial distribution of soil type in the Lan River Basin is similar to that in the Ba River Basin, mainly the loam. Some soils classified as clay and sandy loam are distributed in the upper stream (Fig. 2e). Forest is also the dominant land cover type, while some cultivated lands are located along the river and some grasslands are in the upper stream (Fig. 2f).

Both of the basins are located within the humid climatic zone and the Qinling Mountain, making them having abundant rainfall and steep terrains. Therefore, floods and landslides often occur across the two basins. It is essential and important to develop the prediction capacity of these hazards to reduce and further avoid the damages using the radar and satellite technologies.

2.2. Data

The data used in this study include hourly rainfall rates from the gauge stations, a CINRAD weather radar, and GSMaP satellite products, potential evapotranspiration (PET), digital elevation model (DEM), soil type, land cover type, hourly stream flow records, and landslide inventory. To make data comparable and consistent on the spatial resolution, all gridded data were interpolated or resampled to an identical spatial resolution of 1 km × 1 km (30 arcsec).

Rainfall data used in this study have three sources, including gauge observations, radar QPE and satellite QPE. The hourly observed rainfall, derived from 334 rain gauges (Fig. 1b), were interpolated into gridded data with a spatial resolution of 1 km via the Ordinary Kriging method (Krige, 1951). The period of gauge rainfall is from 00:00UTC Sep. 01 to 23:00UTC Oct. 31, 2017 (*i.e.*, 1464 time steps). Radar QPE was derived from the CINRAD C-band, single-polarization Ankang radar with a radial resolution of 500 m and a detection range of 400 km, which is located at 109.043° E and 32.693° N (Fig. 1a). The radar provided a continuous radar QPE product from 00:00UTC Sep. 22 to 23:00UTC Oct. 7, 2017. The pre-processing of radar QPE data is described in Section 3.1. Satellite rainfall data in this study were from the GSMaP Product (GSMAP_Gauge) of the GPM mission, which are adjusted by National Oceanic and Atmospheric Administration (NOAA) Climate Prediction Center (CPC) Unified Gauge-based Analysis of Global Daily Precipitation. The source precipitation data of GSMaP are obtained by the Passive Microwave and Infrared radiometers retrieval algorithm based on the moving vector with the Kalman filter approach. The temporal resolution of the GSMAP_Gauge data is 1 h, which is averaged from sub-hourly observations of the specified hour. The data has a spatial resolution of 0.1 × 0.1° grid (approximately 10 km at the equator) with a coverage of 60° N to 60° S. To make it comparable to the radar data, these data are interpolated into a spatial resolution of 1 km through the bi-linear interpolation method. Considering the common data availability, we set the time between 00:00UTC Sep. 01, 2017 and 23:00UTC Sep. 21, 2017 as the calibration period and the rest period until 23:00UTC Oct. 31, 2017 as the validation period.

The PET data were retrieved from the hydrological gauge stations and also interpolated into the same grid based on the Ordinary Kriging method. The DEM data are from the Geospatial Data Cloud with a spatial resolution of 90 m. Soil data are from the Harmonized World Soil Database (HWSD) v1.2, which has a spatial resolution of 1 km and contains 13 soil types based on the United States Department of Agriculture (USDA) classification. The land cover type data are from the Climate Change Initiative (CCI) land cover project v2.0. The spatial resolution of this data is 300 m. Streamflow data are used to calibrate the iCRESLIDE model and are from the Hydrological Year Book of the Ministry of Water Resources, China. The landslide inventory data are from the Geological Survey Office of the Department of Land and Resources of Shaanxi Province, with information on the landslide locations, occurrence time, and recorded economic losses.

In this study, the rainfall and PET data are model forcing data, while the DEM, soil type, and land cover type are used to derive background information and model parameters, such as flow direction, flow accumulation, slope angle, soil water capacity, saturate hydraulic conductivity, soil cohesion, porosity, and friction angle. Stream flow discharge and landslide inventory data are for model evaluation.

3. Methodology

3.1. Brief description of the radar QPE algorithm

The Ankang radar of the CINRAD is a C-band, single-polarization Doppler weather radar. We applied a well-studied radar QPE algorithm to retrieve the rainfall rates based on the calibrated relationships between the radar echo intensity (Z) and the precipitation rate (R) since both Z and R are related to the diameter and number of precipitation particles. Based on this, the conversion relationship between Z and R can be established through the drop size distribution (DSD) of rainfall particles (Zhu et al., 2020a; Zhu et al., 2020b), which is referred as the Z-R relationship. In this study, the radar QPE product has 360 azimuths, a radial resolution of 500 m, and a detection range of 400 km. The

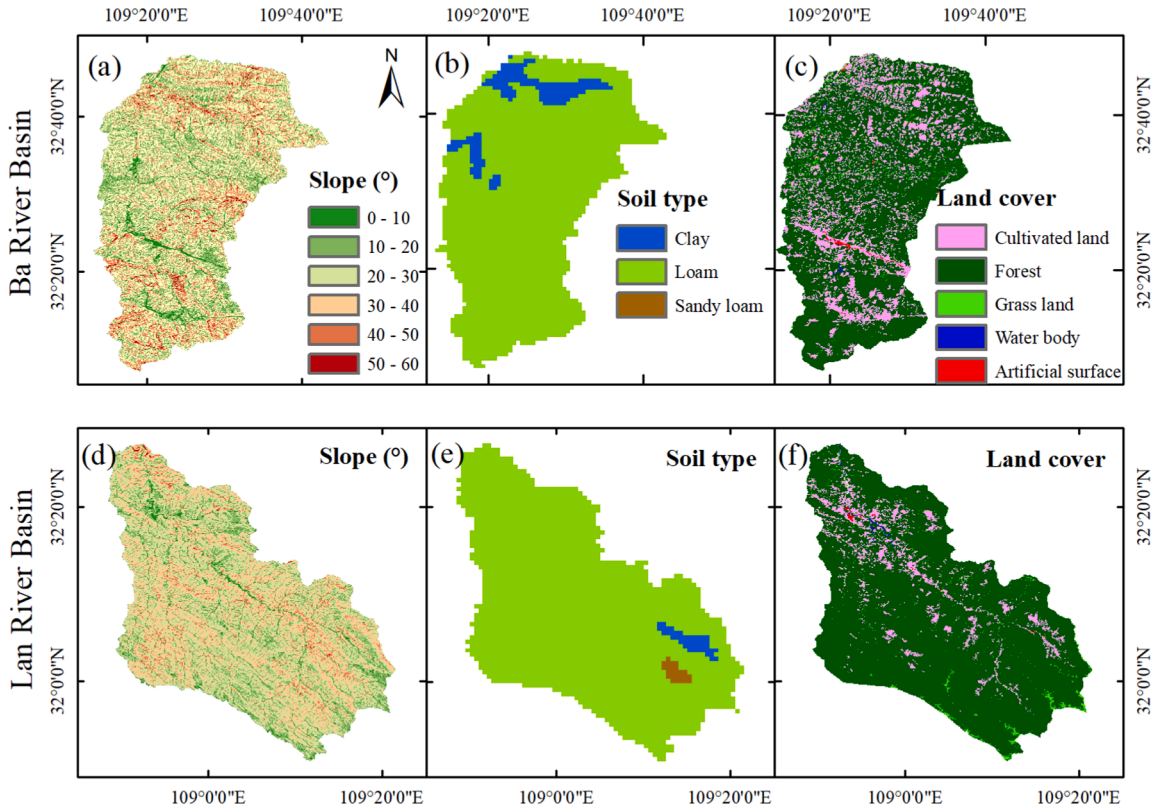

Fig. 2. Spatial maps of slope, soil type, and land cover in the (a-c) Ba River Basin and (d-f) Lan River Basin.

temporal resolution of the radar QPE data is 6 min. To generate the radar QPE under the Cartesian coordinate, the pre-processing procedures are run as follows (Fig. 3): (1) identification of the non-meteorological echoes, such as ground clutter, clear-air echo, super refraction echo, and electromagnetic wave interference echo; (2) compute hybrid elevation angle by considering the occlusion impact of terrain; (3) divide the rainfall into different types by applying a convective-stratiform segregation method based on the vertically integrated liquid (VIL) water (Qi et al., 2013b; Seo et al., 2020; Zhang and Qi, 2010); (4) conduct the vertical profile of reflectivity (VPR) correction, which is very important to reduce overestimation errors caused by bright band in radar QPE (Cao and Qi, 2014; Qi et al., 2013a; Qi et al., 2013b; Qi et al., 2013c; Zhang and Qi, 2010); (5) retrieve the rainfall via different relations of $Z \sim R$ corresponding to different rainfall types; (6) transact the polar coordinate into rectangular coordinate; and (7) accumulate 6 min rainfall rate into hourly radar QPE.

3.2. The iCRESLIDE model

The iCRESLIDE model is proved to have a good performance in flood and landslide prediction not only in basin scale (He et al., 2016) but also in a large region (Wang et al., 2020a). It can simulate the hydrological processes realistically and assess landslide hazards robustly at the same time. Therefore, the iCRESLIDE model was chosen to simulate the flood and landslide hazards in our study.

The iCRESLIDE model contains two parts, the CREST model, which simulate the hydrological processes, and the SLIDE model, which quantifies the stability of slopes. Specifically, the CREST model is a physically based distributed hydrological model that was developed by the University of Oklahoma and NASA (National Aeronautics and Space Administration) SERVIR project team (Wang et al., 2011; Xue et al., 2013). It includes many components concerning hydrological processes, such as the vegetation interception, the infiltration, the soil moisture, and the overland and subsurface flow. Rainfall is intercepted by vegetation canopy before it falls into ground surface. After that, rainfall is partitioned into surface and subsurface runoff based on the infiltration curve, in which the VIC (Variable Infiltration capacity) model is adopted. A routing scheme is proposed to simulate the confluence process where the interactions between routing and runoff generation are considered. The evapotranspiration is deducted throughout all model calculations. The rainfall and PET data with other state parameters are used to force the model, simulating the hydrological processes. A detailed description can be found in the literature (Shen et al., 2016; Wang et al., 2011; Xue et al., 2013; Xue et al., 2016).

The SLIDE model employs a series of mathematical formulations to calculate the slope stability during the time course. The slope stability is expressed as a factor of safety (FS), which is defined as the ratio of resisting forces over destabilizing forces. Lower FS value represents less slope stability. If FS is equal to or less than one, the SLIDE model predicts slope failure. The original SLIDE model takes the entire volume of rainfall into account, neglecting interception and evapotranspiration, which leads to a problem that the rainfall infiltrating into the soil is overestimated dramatically. However, the problem can be fixed by coupling the SLIDE model with a hydrological model in which the vegetation interception and evapotranspiration are included. The detailed description of the SLIDE model can be found in the previous publications (Montrasio and Valentino, 2008).

The two models are mainly linked through the state variable, soil moisture, which is mainly influenced by rainfall infiltration computed by the CREST model. In addition, the CREST model simulation also determines the subsurface water table, which can further affect the slope stability. The SLIDE model is used to assess whether a slope is stable (as the main concern of this study). As the key input of the SLIDE model, soil moisture is computed by the CREST model. The coupling strategy is that the soil moisture simulated by the CREST model is treated as the input of the SLIDE model, which calculates the factor of safety and hence the stability of slope can be judged.

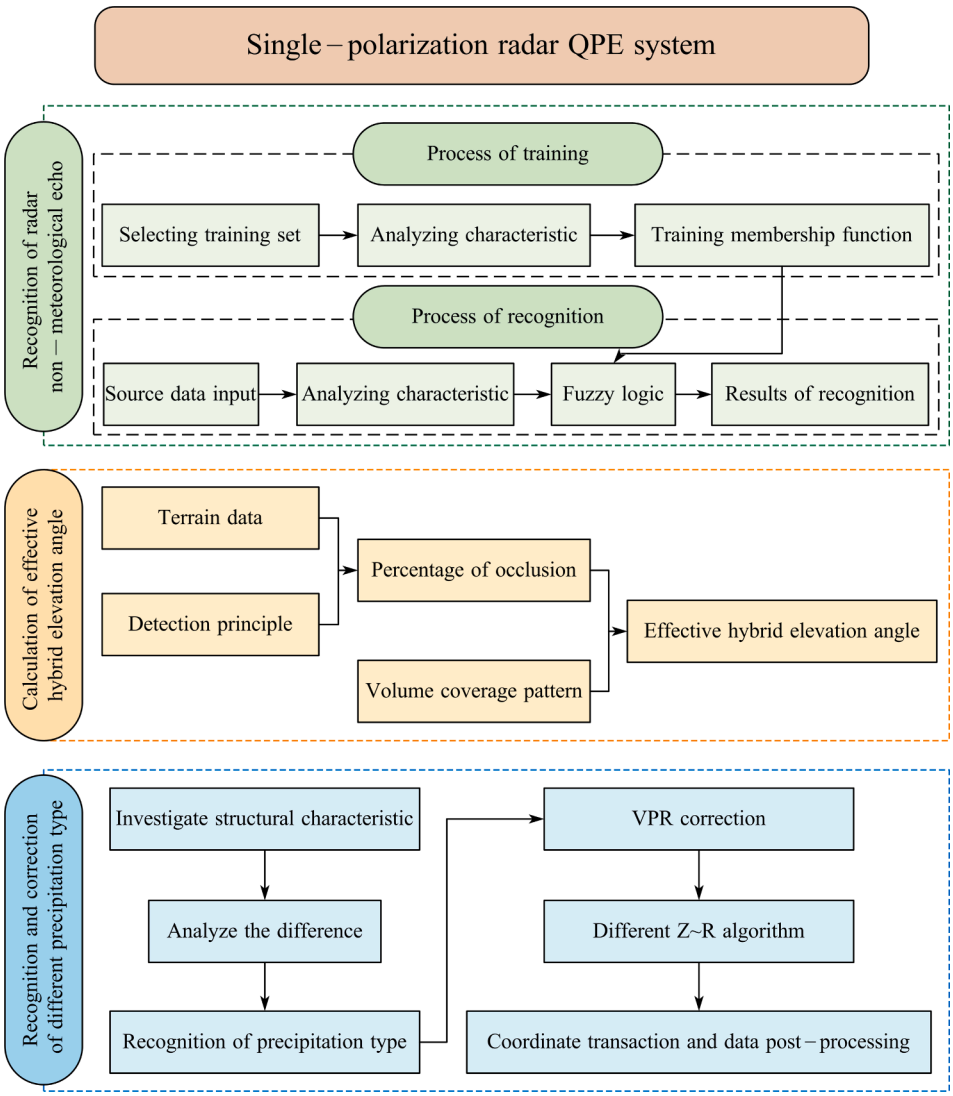

Fig. 3. Flowchart of the radar quantitative precipitation estimation.

3.3. Dynamic correction method for radar and GSMaP satellite QPE

Due to the different detection methods, radar QPE and GSMaP satellite QPE have different accuracies compared to the gauge rainfall (*e.g.*, the radar rainfall may have a smaller uncertainty than satellite). In order to reduce this uncertainty, a suitable correction method should be applied. In this study, we adopted the geographical differential analysis (GDA) method proposed by Cheema (Cheema and Bastiaanssen, 2012) to correct the radar and GSMaP satellite QPEs based on the gauge rainfall because the GDA method takes the difference between gauge rainfall and gridded rainfall (*i.e.*, radar and GSMaP QPEs in our study) into account at a specific location (a gauge station) and hence these point-level biases are interpolated into a spatial map. The interpolation method used in the original GDA method is inverse distance weight (IDW). However, we used the Ordinary Kriging method to do the interpolation in this study because the Ordinary Kriging method can better consider the geophysical difference through a covariance function. The Ordinary Kriging method is widely used in geographical science and atmospheric science.

In previous studies, the time step of correction or calibration for radar and satellite rainfall data was usually one day or one month (Cheema and Bastiaanssen, 2012; Ma et al., 2018b). Considering the time step of model simulation and the limitation of radar rainfall data that only lasts 16 days, we choose six time intervals, which are 3, 6, 12, 24, 48, and 96 hrs, to obtain different sets of bias-corrected rainfall data and to analyze what time interval will lead to a better bias-correction. Here, we named it the Dynamic GDA (DGDA) method. The procedure of DGDA method is summarized as follows:

1. Calculate the bias between radar/satellite QPE and gauge rainfall at the specific locations (*i.e.*, locations of gauge stations) at each chosen time interval (*i.e.*, 3, 6, 12, 24, 48, or 96 hrs). We calculate the difference between gauge rainfall total and radar/satellite QPE rainfall total during the specific time interval as the bias (*e.g.*, if the time interval is set to 3 h, we calculate the bias at each gauge station for every 3 h):

$$\Delta P_{ti} = P_{ti} - P_{rti/sti} \tag{1}$$

where ΔP_{ti} is the difference between gauge rainfall total and radar/satellite QPE rainfall total during the tth time interval at the *ith* station; P_{ti} and $P_{rti/sti}$ are the gauge and radar/satellite rainfall totals during the tth time interval at the *ith* station, respectively.

2. Produce the spatial bias maps (*i.e.*, gridded biases) from the point-level biases at gauge stations for each time interval for the whole period via the Ordinary Kriging method;

3. Partition the gridded biases during each time interval into the gridded biases at each hour according to the ratios of hourly QPE rainfall to QPE rainfall total during each time interval;

4. Correct the hourly biases of the original radar/satellite rainfall data. Considering that the original spatial resolutions of radar and

GSMaP QPE are 1 km and 10 km, respectively, we also conduct the rainfall bias-correction procedure at the 10 km scale. For GSMaP QPE, its native spatial resolution is 10 km, making us able to calculate the spatial biases directly. For radar rainfall, we first aggregated it into the 10 × 10 km resolution and then computed the gridded biases. The rest steps are the same as the above.

3.4. Evaluation metrics of model performance

In order to analyze the impacts of different sources of rainfall on the stream flow simulation, the parameters of the iCRESLIDE model are calibrated first using the gauge rainfall. The same calibrated parameter values are used in the model simulation that are driven by the radar and GSMaP QPEs. The gauge rainfall is as the benchmark in comparison of the radar and GSMaP QPEs, while the model simulations driven by gauge rainfall are used as the benchmark to compare the simulations driven by radar and GSMaP QPEs.

For rainfall comparison, the commonly used metrics including the standard deviation (SD), Pearson correlation coefficient (r), and root mean square error (RMSE) are used to evaluate the accuracy. For the evaluation of the corresponding hydrological simulations, three commonly used metrics, including the relative bias, r, and Nash-Sutcliffe efficiency coefficient (NSE), are used as the performance evaluation metrics. The NSE quantifies the agreement between the simulated discharges and the observed ones. Its value ranges from negative infinity to 1, which can be calculated by following equation:

$$NSE = 1 - \frac{\sum_{t=1}^{T}\left(Q_0^t - Q_m^t\right)^2}{\sum_{t=1}^{T}\left(Q_0^t - \overline{Q_0}\right)^2} \tag{2}$$

where Q_0^t and Q_m^t are the observed and simulated discharge at time t, respectively; $\overline{Q_0}$ is the average value of observed discharge.

The slope stability is assessed by an FS value simulated through the iCRESLIDE model, which is essentially a binary classification model for landslide assessment. For landslide simulation, the output of the coupled model is the FS value, which is compared with a threshold (usually set to 1) to judge whether a slope is unstable. It is a binary classification, which can be evaluated by a receiver operating characteristic (ROC) curve (Fawcett, 2006). To obtain the ROC curve, the model prediction results are classified into four categories, which are the true positive (TP), true negative (TN), false positive (FP) and false negative (FN). TP and FN are the number of instances when a recorded landslide event is correctly predicted to occur and incorrectly predicted to not occur by the model, respectively. TN and FP are the number of instances when no recorded landslide event is correctly predicted to not occur and incorrectly predicted to occur by the model, respectively. Based on the above four quantities, we can evaluate the model performance through the true positive ratio (TPR), true negative ratio (TNR), accuracy, and error rate metrics:

$$\mathrm{TPR} = \frac{\mathrm{TP}}{\mathrm{TP} + \mathrm{FN}} \tag{3}$$

$$\mathrm{TNR} = \frac{\mathrm{TN}}{\mathrm{TN} + \mathrm{FP}} \tag{4}$$

$$\mathrm{accuracy} = \frac{\mathrm{TP} + \mathrm{TN}}{\mathrm{TP} + \mathrm{TN} + \mathrm{FP} + \mathrm{FN}} \tag{6}$$

$$\mathrm{errorrate} = 1 - \mathrm{accuracy} \tag{7}$$

By varying the FS threshold, we can compute a series of TPR and TNR pairs to form the ROC curve. The model performs well if the ROC curve is close to the upper-right corner. The area under the ROC curve (AUC) reflects the overall accuracy of the model simulation; a higher AUC means a more accurate model simulation.

4. Results

4.1. Uncertainty and its correction in the radar and GSMaP QPEs

In order to analyze the radar and GSMaP QPEs, the cumulated rainfall of gauge, radar and GSMaP rainfall were calculated for the period of Sep. 22 to Oct. 07, 2017 at each 1-km grid cell containing a rain gauge. Fig. 4 shows the scatter density plots of the cumulated radar and GSMaP rainfall comparing to the cumulated gauge observations. As shown in Fig. 4, both radar QPE and GSMaP QPE have a low accuracy comparing to the gauge observations indicated by the low values of r and high values of RMSE (Fig. 4). In addition, radar QPE tends to underestimate the rainfall with an average bias of −0.457 mm (Fig. 4a), while GSMaP QPE overestimates the rainfall with an average bias of 0.498 mm (Fig. 4b). Relatively, the GSMaP QPE has a slightly better accuracy than the radar QPE indicated by the r, RMSE, and bias metrics. These results clearly demonstrate that considerable uncertainty exists in both radar and GSMaP QPEs in this case. Therefore, bias-correction is necessary to improve their quality.

To reduce uncertainty in radar and GSMaP rainfall data, the DGDA correction method based on the gauge rainfall data is conducted. Fig. 5 shows the scatter density plots of the cumulated radar bias-corrected rainfall (Fig. 5a-5f) and the cumulated GSMaP bias-corrected rainfall (Fig. 5g-5 l) compared to the cumulated gauge rainfall at the site scale. Comparing to the original radar and GSMaP QPEs data, the bias-corrected radar and GSMaP QPEs are significantly improved and agree much better with the gauge observations (Fig. 5). All of the three metrics in the bias-corrected QPEs (Fig. 5) are all largely improved relative to those in the original QPEs (Fig. 4), indicating that the bias-correction method is totally effective. In addition, the effectiveness of the DGDA bias-correction method is clearly dependent on the correction time interval. As shown in Fig. 5a-5f, the bias metric of the bias-corrected radar QPE is first reduced from 0.133 mm to −0.012 mm when the correction time interval is increased from 3 hrs to 24 hrs and then increased as the time interval is increased from 24 hrs to 96 hrs. The RMSE metric of the bias-corrected radar QPE also shows a relationship with the time interval similar to the bias-time interval relationship (Fig. 5a-5f): RMSE of the bias-corrected radar QPE is first reduced from 50.839 mm to 38.958 mm as the correction time interval is increased from 3 hrs to 24 hrs and then increased as the time interval is increased from 24 hrs to 96 hrs (Fig. 5a-5f). In contrast, the r metric of the bias-corrected radar QPE increases first and then decreases as the time interval increases, with the highest value as time interval is set to 24 hrs (Fig. 5d). These results suggest that simply extending the correction time interval does not necessarily reduce the error spread in the bias-corrected radar QPE. When the correction time interval is set between 12 hrs and 24 hrs, the overall performance of the bias-correction for the radar QPE in this case reaches the optimal indicated by the three metrics. For the bias-correction of the GSMaP QPE, bias metric of the GSMaP bias-corrected QPE is reduced first and then increased as the correction time interval increases (Fig. 5g-l). The RMSE metric of the GSMaP bias-corrected QPE is slightly increased as the time interval is increased from 3 hrs to 12 hrs and then gradually reduced as the time interval is increased from 12 hrs to 48 hrs (Fig. 5g-5 k). The r metric is first increased as the time interval is increased from 3 hrs to 12 hrs and then decreased as the time interval is increased, which is similar to the RMSE-time interval relationship (Fig. 5g-l). Both of the bias and RMSE statistics reach the lowest value when the time interval is set to 48 hrs (Fig. 5k). The overall performance of the bias-correction for the GSMaP QPE in this case reaches an optimal performance when the correction time interval is set between 12 hrs and 48 hrs.

Taylor diagram is usually used in the analysis of meteorology data and can compare the SD, RMSE and r metrics at the same time. The Taylor diagrams of the cumulated radar bias-corrected rainfall and the cumulated GSMaP satellite bias-corrected rainfall using six time intervals comparing to the cumulated gauge rainfall at the site scale are

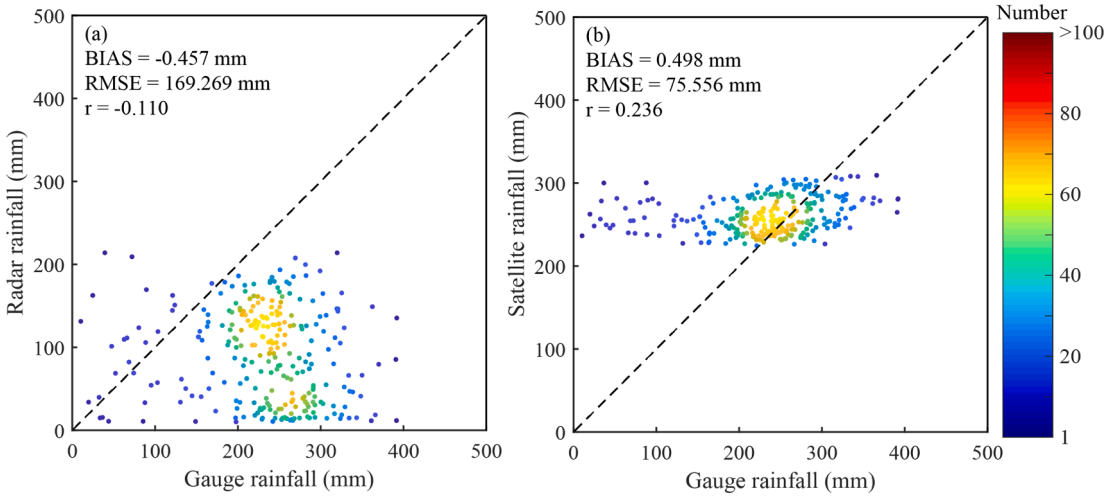

Fig. 4. Scatter density of comparisons of (a) the cumulated gauge rainfall vs. the cumulated radar rainfall and (b) the cumulated gauge rainfall vs. the cumulated GSMaP satellite rainfall at the site scale from Sep. 22 to Oct. 7, 2017.

shown in Fig. 6a and Fig. 6b, respectively. In addition, we also compared the hourly regional average bias-corrected radar and GSMaP rainfall data sets with the hourly station-based regional average rainfall from 00:00UTC Sep. 22 to 23:00UTC Oct. 7, 2017 (Fig. 6c and 6d). In Fig. 6, A is the gauge observation, while B, C, D, E, F, and G presents the bias-corrected results using the correction time intervals of 3, 6, 12, 24, 48, and 96 hrs, respectively. On the site-level comparison that quantifies the agreement of the bias-corrected QPEs with the observations on the spatial patterns, the results of both in radar and GSMaP produced by the different correction time intervals are generally close to each other. Relatively speaking, the results based on the correction time intervals of 6, 12, and 24 hrs (*i.e.*, C, D, and E in Fig. 6a) for the radar QPE have gained a better quality than the results based on the other correction intervals. Similar but slightly different the radar results, the results based on the correction time intervals of 6, 12, 24, and 48 hrs (*i.e.*, C, D, E, and F in Fig. 6b) for the GSMaP QPE have gained a better quality than the other results. Since the DGDA bias-correction method is implemented at each gauge station, the bias correction can gain good results on different correction time intervals. In contrast, differential bias-correction performance appears on the regional-level comparison, which measures the agreement of the bias-corrected QPEs with the observations over the time. The results of bias-corrected radar QPEs using the correction time intervals of 12 and 24 hrs (D and E in Fig. 6c) are clearly better than the other results. However, bias-correction for GSMaP QPE achieves are better performance when the correction time intervals are set to 24, 48, and 96 hrs (E, F and G in Fig. 6d).

To investigate the performance of bias-correction on the correction of hourly rainfall data, we further compared the bias-corrected hourly radar and GSMaP QPEs with the observations at the site level (Fig. 7). The bias metric of the bias-corrected hourly radar QPE is first reduced from 21.933 mm to 11.388 mm as the time interval is increased from 3 hrs to 12 hrs, and is then continuously increased as the time interval is increased from 12 hrs to 96 hrs (Fig. 7a-7f). The RMSE metric of the bias-corrected hourly radar QPE is also first decreased as the time interval is increased from 3 hrs to 24 hrs, and is then increased as the time interval is increased from 24 hrs to 96 hrs (Fig. 7a-7f). The r statistic is first increased from 0.479 to 0.722 as the time interval is increased from 3 hrs to 12 hrs (Fig. 7a-7c), and is then decreased as the time interval is increased from 12 hrs to 96 hrs (Fig. 7d-7f). It is obvious that the bias correction can achieve the best results for the hourly bias-corrected radar QPE when the correction time interval is set between 12 hrs and 24 hrs. Regarding the GSMaP correction performance, the bias metric of the bias-corrected hourly GSMaP QPE is first increased as the time interval is increased from 3 hrs to 12 hrs, and is then decreased from 12 hrs to 96 hrs (Fig. 7g-7 l). As the time interval is increased from 3 hrs to 48 hrs, the RMSE and r statistics are decreased and increased, respectively; both of the two metrics reach their best values when time interval is equal to 48 hrs (Fig. 7k). It is clear that bias-correction for the GSMaP QPE can achieve the best results when the time interval is set between 24 hrs and 48 hrs (Fig. 7j-7 k).

Overall, the bias-correction for radar and GSMaP QPEs using the 24 hrs correction time interval can achieve an optimal result in terms of better capturing the both spatial and temporal variability of the observations. Therefore, the bias-corrected rainfall of radar and GSMaP using the 24 hrs time interval are selected to drive the iCRESLIDE model for further analysis and hence analyze the impacts of original and corrected rainfall on the model simulations.

4.2. *Hydrological evaluation of the original and bias-corrected radar and GSMaP QPEs*

To analyze the utility of original radar and GSMaP QPEs and the effectiveness of the QPE bias correction, we compared the simulated discharge driven by the gauge rainfall, radar QPE, GSMaP QPE, bias-corrected radar QPE, and bias-corrected GSMaP QPE with the observed discharge at the outlets of the basins. Fig. 8 shows the cumulated stream flow discharge over time for all simulations and the observation. The results in the Ba River Basin (Fig. 8a) are similar to those in the Lan River Basin (Fig. 8b). First, the original GSMaP QPE-driven discharges are apparently overestimated comparing to the observations in the two basins (green solid lines in Fig. 8a and 8b) due to the positive biases in the GSMaP QPE (Fig. 4b), while the original radar QPE-driven discharges are clearly underestimated in both of the basins (blue solid lines in Fig. 8a and 8b) because of the negative biases in the radar QPE (Fig. 8a). In contrast, the simulated discharges driven by the bias-corrected radar (blue dashed lines in Fig. 8a and 8b) and GSMaP (green dashed lines in Fig. 8a and 8b) rainfall agree very well with the observed discharge (black lines in Fig. 8a and 8b) and the simulated discharge driven by the gauge observations (red lines in Fig. 8a and 8b) in the two basins, indicating that bias correction substantially improves the performance of the model, which is critical for flood simulation and prediction. The simulated discharges driven by the gauge observations (red lines in Fig. 8a and 8b) agree well with the observed ones (black lines in Fig. 8a and 8b) in both of the basins, indicated by the NSE values of 0.778 and 0.743, respectively. These results suggest that the iCRESLIDE model has a capability of capturing the hydrological processes. The NSE values of the iCRESLIDE model driven by the original radar and GSMaP QPEs are 0.347 and 0.368 in the Ba River Basin, respectively

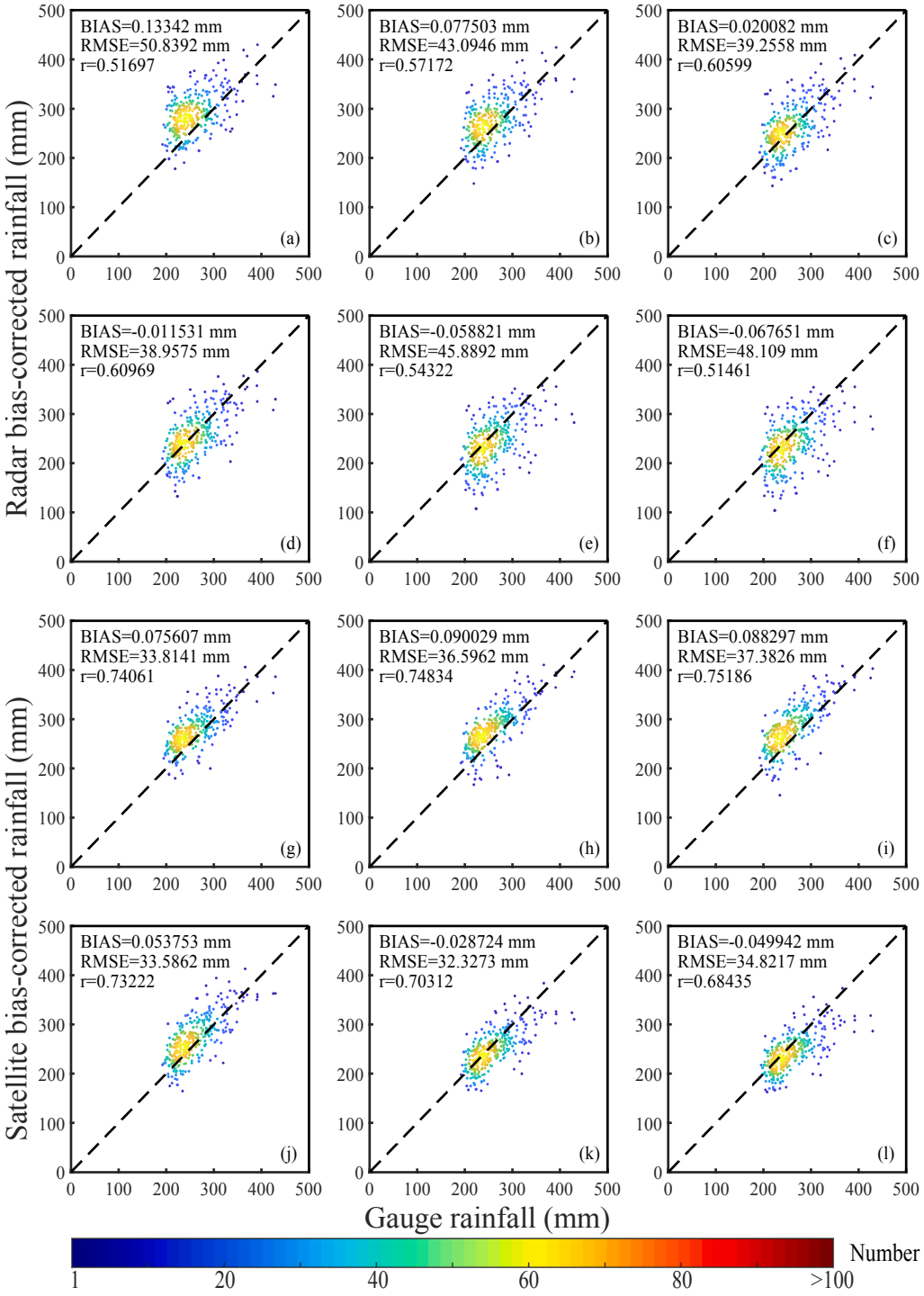

Fig. 5. Comparisons of (a-f) the cumulated gauge rainfall vs. the six sets of cumulated radar bias-corrected rainfall and (g-l) the cumulated gauge rainfall vs. the six sets of cumulated GSMaP satellite bias-corrected rainfall at the site scale from Sep. 22 to Oct. 7, 2017; bias-corrections for radar and GSMaP satellite data were conducted six times to produce six sets of bias-corrected data using the correction time intervals of 3 hrs, 6 hrs, 12 hrs, 24 hrs, 48 hrs, and 96 hrs, respectively.

(Fig. 8a) and 0.105 and −0.406 in the Lan River Basin, respectively. These results are not satisfactory and demand an improvement to achieve a better prediction. Once the DGDA bias correction is applied, the NSE metrics of the results driven by the bias-corrected radar QPEs reach 0.718 and 0.676 in the two basins, while the NSE values of those driven by the bias-corrected GSMaP QPEs are 0.727 and 0.802 in the two basins.

To further compare the performance of model simulations forced by different rainfall data, the NSE, relative bias, and r metrics are calculated and summarized in Table 1. The results driven by the uncorrected rainfall data apparently have lower qualities, with lower NSE values (<0.40) and higher absolute relative biases (up to 65.275% and 42.784% for the radar and GSMaP results, respectively), indicating that the original radar and GSMaP indeed contain considerable uncertainty in this region. This region has a complex and steep terrain, which may largely impair the accuracy of the radar and satellite rainfall retrieval algorithms. However, once the bias-correction is applied, the model results driven by the bias-corrected radar and GSMaP rainfall achieved a

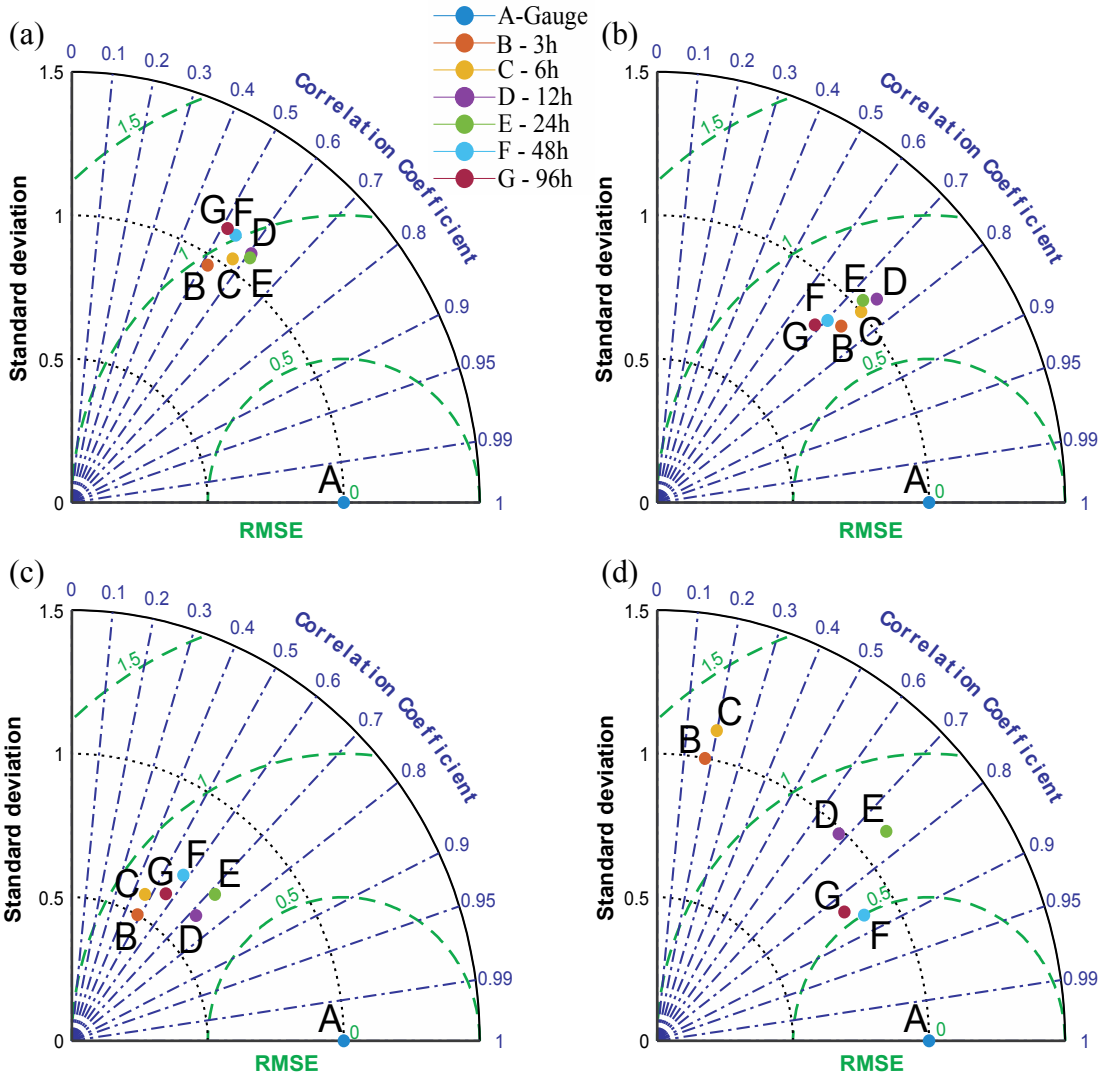

Fig. 6. Taylor diagrams of (a) the cumulated radar bias-corrected rainfall and (b) the cumulated GSMaP satellite bias-corrected rainfall using six correction time intervals comparing to the cumulated gauge rainfall at the site scale and (c) the regional average hourly radar bias-corrected rainfall and (d) the regional average hourly GSMaP satellite bias-corrected rainfall using six correction time intervals comparing to the observations.

much better performance with the NSE values $\geq$ 0.676, the absolute values of the relative bias $\leq$ 17.126%, and the r values $\geq$ 0.753 (Table 1). Relatively, the results driven by the bias-corrected radar rainfall are generally better than those driven by bias-corrected GSMaP rainfall in the Ba River Basin, indicated by the higher NSE and the lower relative bias. In contrast, the model results driven by the bias-corrected GSMaP QPE are slightly better than those driven by the bias-corrected radar QPE in the Lan River Basin (Table 1).

4.3. Evaluation of the utility of the original and bias-corrected radar and GSMaP QPEs for landslide prediction

The landslide inventory recorded that three landslide events occurred in each of the two basins during the period of Sep. 22 to Oct. 07, 2017. To evaluate the simulation results driven by different sources of rainfall, 30 grid cells without reported landslides were randomly selected. Fig. 9 shows the FS values of the model simulations driven by gauge, radar, GSMaP, bias-corrected radar, and bias-corrected GSMaP rainfall. The red dashed line in Fig. 9 represents the critical value of slope stability (*i.e.*, FS = 1). A lower value than 1 (*i.e.*, below the red dashed line) indicates an unstable slope (*i.e.*, a modeled landslide event), while a higher value than 1 (*i.e.*, above the red dashed line) denotes a stable slope (*i.e.*, model predicts no landslide occurring). The vertical blue dash line in Fig. 9 separates the six grid cells with reported landslide events from these randomly selected grid cells without reported landslides.

The simulation driven by the gauge observations correctly predicts four of the six landslide events (Fig. 9) with a true positive ratio (TPR) of 66.7% and a true negative ratio (TNR) of 83.3% (Table 2), indicating that the iCRESLIDE model has an overall predictive capability for the slope stability when it is forced by the observed rainfall. It is not surprise that the simulations driven by the original radar and GSMaP QPEs have downgraded performances than the simulation driven by the observed rainfall (Fig. 9 and Table 2). The TPR values for the simulations driven by the original radar and GSMaP QPEs are 33.3% and 50%, respectively, while the TNR values are 83.3% and 76.7%, respectively. Both of the simulations driven by the original radar and GSMaP QPEs have high error rates that are 25–27.8% (Table 2). The rainfall bias correction has substantially improved the landslide prediction, increased the TPRs of the radar and GSMaP based results by 16.7% and 16.7%, respectively (Table 2), and reduced the error rates of the radar and GSMaP based results by 11.1% and 13.9%, respectively (Table 2). These results suggest that accuracy in the rainfall forcings is critical for the accurate prediction of landslides and the bias-correction improves the accuracy of

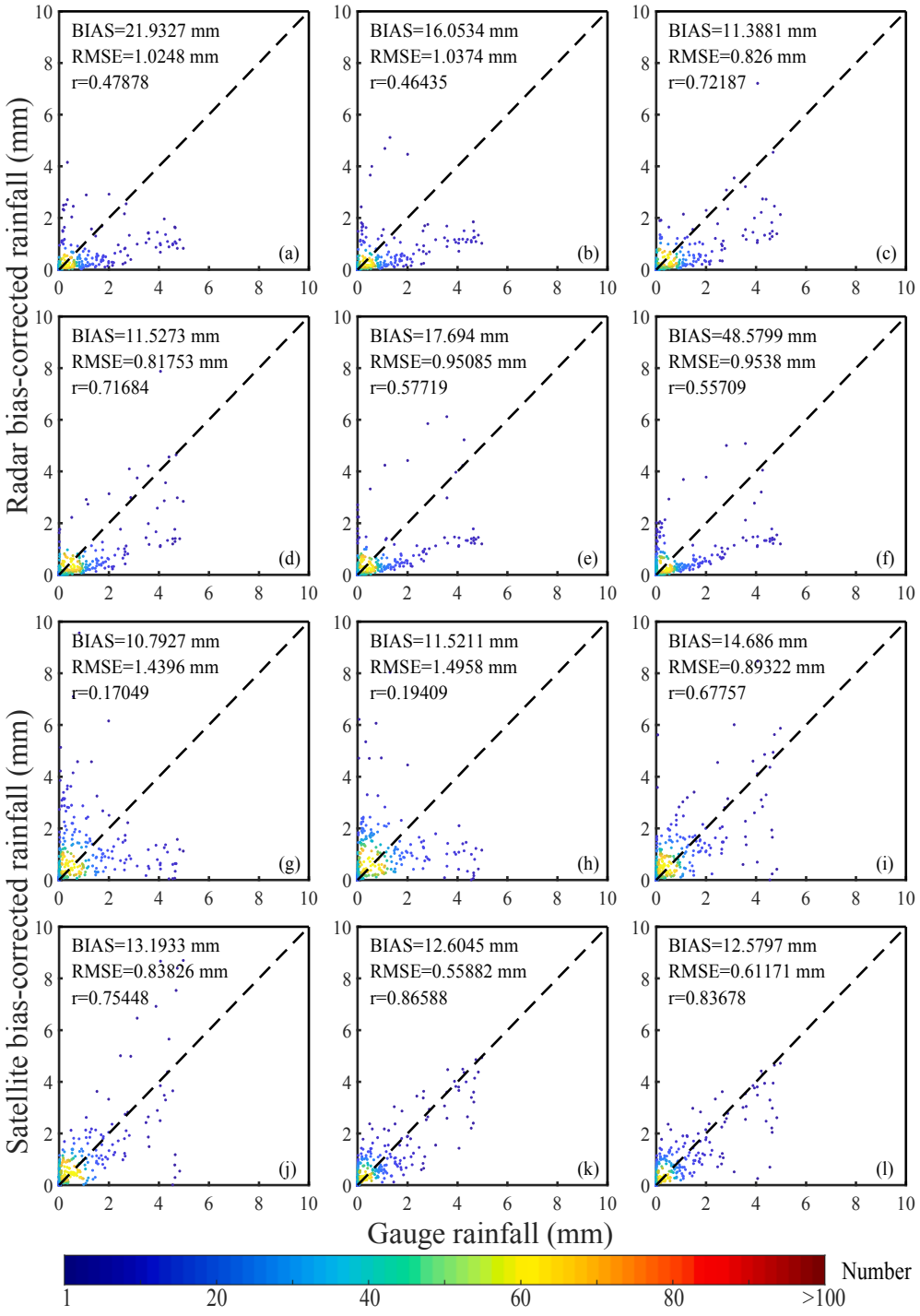

Fig. 7. Comparisons of (a-f) the regional average gauge rainfall vs. the six sets of regional average radar bias-corrected rainfall and (g-l) the regional average gauge rainfall vs. the six sets of regional average GSMaP satellite bias-corrected rainfall at the hourly scale from Sep. 22 to Oct. 7, 2017; bias-corrections for radar and GSMaP satellite data were conducted six times to produce six sets of bias-corrected data using the correction time intervals of 3 hrs, 6 hrs, 12 hrs, 24 hrs, 48 hrs, and 96 hrs, respectively.

radar and satellite rainfall, leading to better performance of model simulation and improving the predictive capability of the iCRESLIDE model for landslides.

To further analyze the accuracy of landslide prediction, the ROC curves of the simulations driven by the five sets of rainfall data are also derived (Fig. 10). It is clear that the ROC curves of the simulations driven by the bias-corrected rainfall data are closer to the upper-right corner than those of the uncorrected rainfall. The rainfall bias correction makes the AUC value of the ROC curve increase from 0.633 to 0.767 and from 0.619 to 0.803 for the radar case and GSMaP case, respectively. More important, the results driven by the bias-corrected rainfall are close to these driven by the gauge observations. The AUC values for the bias-corrected radar and bias-corrected GSMaP driven cases, (0.767 and 0.803, respectively) are even higher than that for the gauge driven case (AUC = 0.738).

4.4. The impacts of gauge density and spatial resolution of QPEs on the effectiveness of bias correction

Considering that the application of the DGDA method would be dependent on the gauge density and spatial resolution, we further analyzed the impacts of gauge density and spatial resolution of QPEs on the effectiveness of bias correction. In this study, the total number of gauge stations is 334 with a station density of 1.242 stations per 100

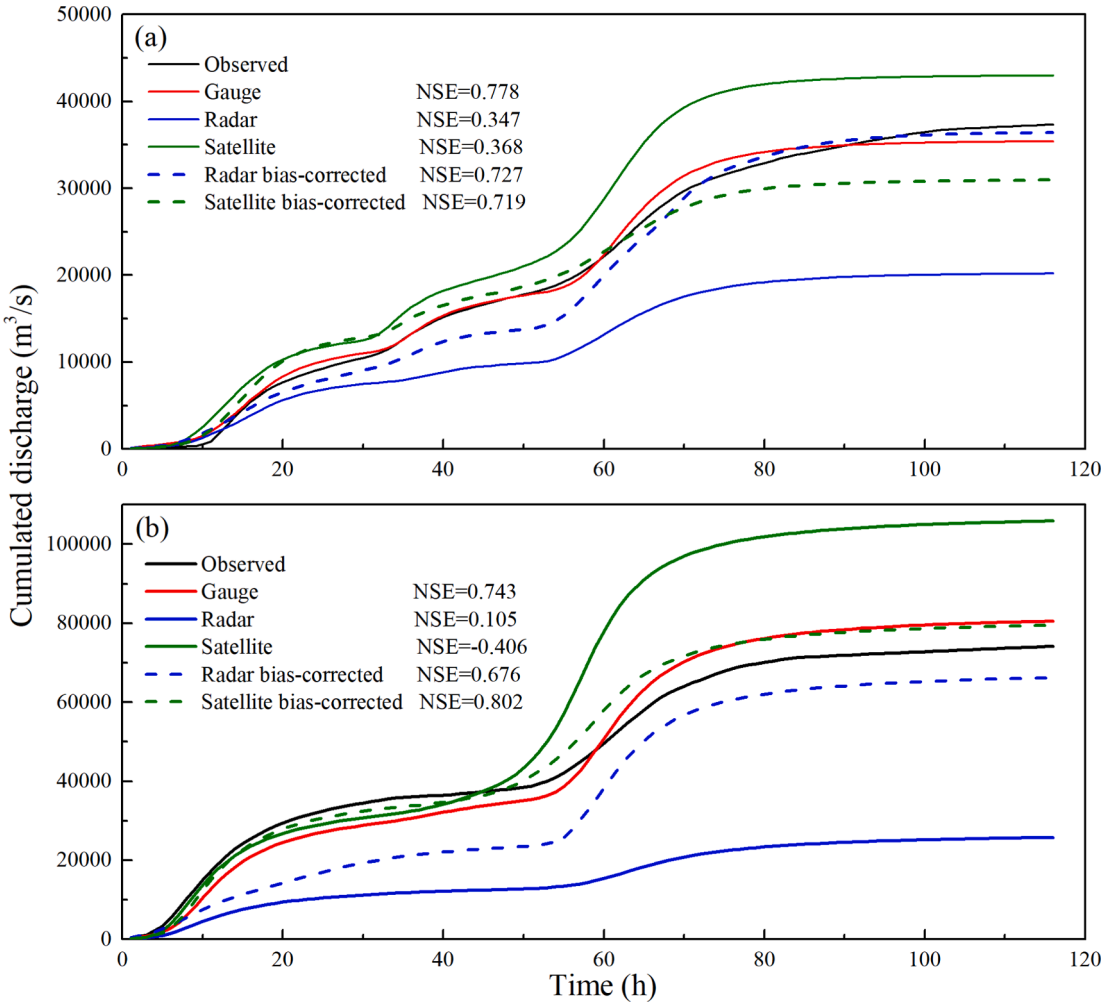

Fig. 8. Cumulated discharges forced by gauge, radar, GSMaP satellite, radar bias-corrected and GSMaP satellite bias-corrected rainfall data in the (a) Ba River Basin and (b) Lan River Basin.

Table 1
Performance summary of the iCRESLIDE simulated discharges during the Sept 22-Oct 7, 2017 period in the study basins.

Basins	Rainfall forcings	NSE	Relative bias (%)	r
Ba River	Gauge	0.778	−5.205	0.928
	Radar	0.347	−45.956	0.858
	GSMaP	0.368	15.069	0.884
	Bias-corrected radar	0.727	−2.493	0.817
	Bias-corrected GSMaP	0.719	−17.126	0.890
Lan River	Gauge	0.743	8.541	0.903
	Radar	0.105	−65.275	0.891
	GSMaP	−0.406	42.784	0.758
	Bias-corrected radar	0.676	−10.760	0.753
	Bias-corrected GSMaP	0.802	7.235	0.919

km^2. To further analyze the impact of the station density on the rainfall correction performance, we conducted the rainfall correction procedure by randomly excluding 25%, 50%, 75% and 90% of the total stations, which resulted in a station density of 0.930, 0.621, 0.309 and 0.123 stations per 100 km^2, respectively. The threshold of gauge density recommended by the World Meteorological Organization (WMO) is one gauge per 575 km^2 (Gadelha et al., 2019), *i.e.*, 0.174 stations per 100 km^2. The station densities by randomly excluding 25%, 50%, and 75% of the total stations in this study can result in a higher gauge density than the WMO recommended gauge density, while the resultant station density by randomly excluding 90% of the total are lower than the WMO recommended gauge density. These results suggest that our experiments on the impacts of different station densities cover a wide range of station density and are sufficient to analyze the relationship between bias correction and gauge density. To reduce the uncertainty in the random station-excluding procedure, we conducted 10 repeated trials each time and calculated their average value to quantify the performance of the bias-correction method. The statistical metrics used to quantify the performance of bias correction include the relative bias (*i.e.*, the ratio of the absolute bias with some stations excluded to the absolute bias with all gauge stations included), relative RMSE (*i.e.*, the ratio of the RMSE with some stations excluded to the RMSE with all gauge stations included), and r. As the number of stations, or the station density, decreases, the RMSE and r metrics are downgraded gradually for both radar (Fig. 11a) and GSMaP (Fig. 11b) cases. However, the relative bias metric does not show a monotonic relationship with the station density (Fig. 11a and 11b). These results highlight the importance of station density or station representativeness on achieving good bias correction, which agree with the findings by Tang et al. (2018) and Gadelha et al. (2019) that the performance of gauge observation-based radar/satellite bias correction is dependent on the gauge density. Although the station density is important for the bias correction, observations from even a small number of stations will be helpful for improving the quality and GSMaP QPEs.

To detect the impacts of different spatial resolutions on the rainfall bias correction, we further conducted the rainfall correction at the spatial resolution of 10 km × 10 km, which is the same spatial resolution

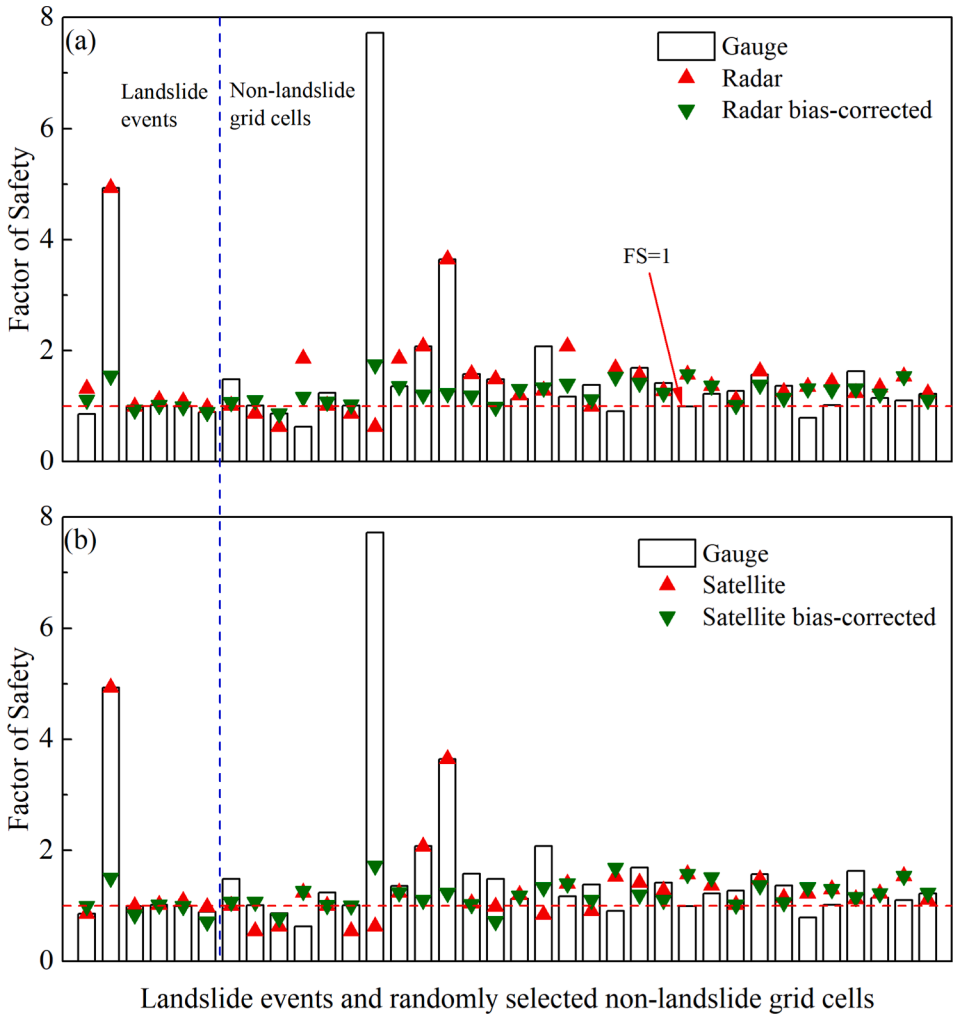

Fig. 9. Simulated FSs of the grid cells with reported landslides and randomly selected non-slide grid cells driven by (a) gauge, radar, and radar bias-corrected rainfall, and (b) gauge, GSMaP satellite, and GSMaP satellite bias-corrected rainfall in the two basins.

Table 2
Evaluation metrics of the landslide predictions driven by the five rainfall data.

Metrics	Gauge driven	Radar driven	GSMaP driven	Bias-corrected Radar driven	Bias-corrected GSMaP driven
TPR	66.7%	33.3%	50%	50%	66.7%
TNR	83.3%	83.3%	76.7%	93.3%	90%
Accuracy	80.6%	75%	72.2%	86.1%	86.1%
Error rate	19.4%	25%	27.8%	13.9%	13.9%

of the original GSMaP QPE. To match with the 10 km × 10 km spatial resolution, we aggregated the 1-km radar QPE to 10 km. It is clear that the r-values for the results with a finer resolution are higher than those with a coarser resolution and the RMSE values for the results with a finer resolution are lower than those with a coarser resolution (Fig. 12), indicating that the spatial resolution matters for the bias correction. However, the biases for the results with a finer resolution are slightly higher than those with a coarser resolution (Fig. 12).

5. Conclusions and discussion

In this study, we investigated the utility of the C-band, one-polarization radar QPE and the GSMaP satellite QPE of the GPM mission for the integrated prediction of floods and landslides, developed a dynamic bias correction to reduce uncertainty in radar and satellite

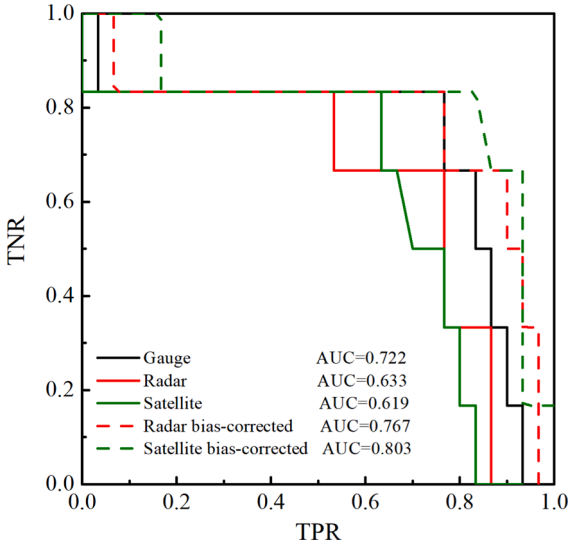

Fig. 10. The ROC curve forced by gauge, radar, GSMaP satellite, radar bias-corrected and GSMaP satellite bias-corrected rainfall data.

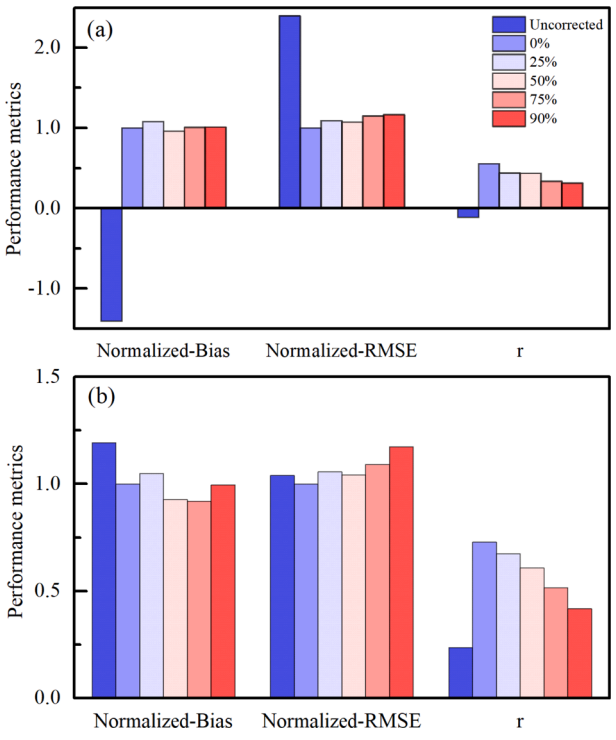

Fig. 11. Normalized-Bias, normalized-RMSE and r values of (a) radar bias-corrected and (b) GSMaP satellite bias-corrected rainfall using the bias correction procedure with a fraction of gauge stations randomly excluded (*e.g.*, 25% refers to randomly excluding 25% of the total gauge stations) compared with the gauge rainfall.

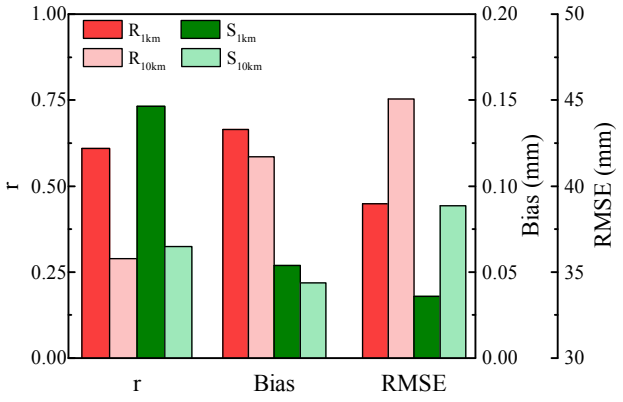

Fig. 12. Metric values of radar bias-corrected and GSMaP satellite bias-corrected rainfall compared with the gauge rainfall at spatial resolutions of 1 km and 10 km (R_{1km} is the radar bias-corrected rainfall at 1 km spatial resolution while R_{10km} is at 10 km spatial resolution; the same abbreviations for satellite bias-corrected rainfall).

QPEs using gauge observations, and explored the impacts of gauge density and spatial resolution of QPE on the effectiveness of bias correction in two hilly basins of southern Shaanxi Province of China. This study highlights several valuable findings. First, both the C-band, one-polarization radar QPE and GSMaP satellite QPE provide valuable real-time or quasi real-time rainfall data for this region that can be used by the model to predict the flood and landslide hazards, although these QPEs have considerable uncertainty that need be reduced. Second, the developed dynamic bias correction method is effective to reduce the uncertainty in the radar and satellite QPEs and further largely improves the accuracy of near real-time rainfall monitoring and hence predictive accuracy of the iCRESLIDE model for predicting both flood and landslide hazards. Finally, although the station density and spatial resolution matters for the bias correction, inclusion of the observations from even a small number of rain gauges will be helpful for reducing the uncertainty in the radar and satellite QPEs. The bias correction method developed in this study and the findings will be useful for the similar studies and provide valuable guidance for further developing the QPE algorithms and multi-source precipitation merging methods.

In addition, several findings in our study need be paid more attention. Our results find that the original radar QPE in this region is not very accurate and even has a slightly lower accuracy than the GSMaP QPE. Several factors can contribute to the relatively low accuracy of the radar QPE. First, this region has a complex terrain and dense vegetation, which may affect the rainfall detection of the radar. In addition, this radar is one-polarization radar, which limits its ability to gain better QPE. However, with the aid of sufficient gauge stations, we can substantially reduce the uncertainty in the radar and GSMaP QPEs. Multi-source precipitation merging method will be important way to improve the precipitation quality (Chao et al., 2018; Ma et al., 2018a; Sivasubramaniam et al., 2019). Although gauge station density is a critical factor on the accuracy of multi-source precipitation merging, however, it is difficult or infeasible in reality to build a large amount gauge stations everywhere, especially in the mountainous areas, due to the limitation of construction and finance. An effective way to solve this problem is to develop new techniques and approaches to quantify the spatiotemporal uncertainty in the radar and GSMaP QPEs and/or jointly utilize different observational or sensing platforms (Chen et al., 2019; Le et al., 2020; Tavakol-Davani et al., 2013). The improvement of the radar and GSMaP QPEs will not only provide higher accuracy rainfall data, but also improve the performance of integrated prediction of flood and landslide hazards.

As a critical forcing data of the hydrological models, rainfall significantly affects the accuracy of the simulated discharge (Chao et al., 2018). Overestimation (underestimation) of rainfall usually leads to overestimated (underestimated) flood and landslide hazards. In this study, the Ankang radar QPE and GSMaP satellite QPE tends to underestimate and overestimate the rainfall storm in our study area during the Sept. 22-Oct. 7, 2017 period, respectively. As a result, they caused underestimated and overestimated hydrological processes, respectively. However, with the aid of the DGDA bias correction method, the performance of discharge simulation is largely improved, confirming the effectiveness of the rainfall correction method. On the other hand, the flood simulation result of radar bias-corrected rainfall is slightly better than that of satellite bias-corrected rainfall, illustrating that radar rainfall with a higher native spatial resolution and can better represent the spatial patterns of rainfall. In addition, the bias-corrected radar rainfall obtained higher NSE and r values and a lower bias value on flood simulation than the bias-corrected GSMaP rainfall in Ba River Basin, but the simulations driven by the bias-corrected GSMaP rainfall gains a slightly better result than those driven by the bias-corrected radar rainfall in the Lan River Basin. Relative to the Ba River Basins, the Lan River Basin has a more complex terrain. This illustrates that although the DGDA method can improve the accuracy of radar and GSMaP satellite rainfall data, the representativeness of the gauge data matters for the effectiveness of bias correction.

Another issue is that our study period is relatively short (16 days in autumn) due to the limited availability of radar QPE. The results concluded from this short-period study may be biased and different from the rainfall correction results for a longer period, because the short-period rainfall events could be caused by a specific storm system (*e.g.*, typhoon). The bias-correction method should be further validated in the other seasons (*e.g.*, spring and winter), on a longer time period, and in the other places to assess the robustness of the DGDA method. We believe that the above-mentioned continuing studies will certainly draw a more solid conclusion on the performance and reliability of this developed bias-correction method.

CRediT authorship contribution statement

Sheng Wang: Conceptualization, Formal analysis, Methodology, Investigation, Methodology, Writing original draft, Writing - review & editing, Visualization, Validation. **Ke Zhang:** Conceptualization, Formal analysis, Methodology, Investigation, Funding acquisition, Methodology, Writing - original draft, Writing - review & editing. **Lijun Chao:** Methodology. **Donghuan Li:** Data curation, Writing - review & editing. **Xin Tian:** Writing - review & editing. **Hongjun Bao:** Data curation. **Guoding Chen:** Visualization, Validation. **Yi Xia:** Visualization, Validation

Declaration of Competing Interest

The authors declare that they have no known competing financial interests or personal relationships that could have appeared to influence the work reported in this paper.

Acknowledgement

The first author wants to thank Master student Ran Tao for helping the digitization of flood data. This work was supported by the National Natural Science Foundation of China (51879067), National Key Research and Development Program of China (2016YFC0402701 and 2018YFC1507505), Fundamental Research Funds for the Central Universities of China (B200204038), Hydraulic Science and Technology Plan Foundation of Shaanxi Province (2019slkj-B1), Natural Science Foundation of Jiangsu Province (BK20180022), Hydraulic Science and Technology Plan Foundation of Jiangsu Province (2018055), and Six Talent Peaks Project in Jiangsu Province (NY-004).

References

Atlas, D., Rosenfeld, D., Wolff, D.B., 1990. Climatologically tuned reflectivity-rain rate relations and links to area-time integrals. J. Appl. Meteorol. 29 (11), 1120–1135.
BEVEN, K.J., KIRKBY, M.J., 1979. A physically based, variable contributing area model of basin hydrology/Un modèle à base physique de zone d'appel variable de l'hydrologie du bassin versant. Hydrol. Sci. J. 24 (1), 43–69.
Blöthe, J.H., Korup, O., Schwanghart, W., 2015. Large landslides lie low: Excess topography in the Himalaya-Karakoram ranges. Geology 43 (6), 523–526.
Bogaard, T., Greco, R., 2018. Hydrological perspectives on precipitation intensity-duration thresholds for a landslide initiation: proposing hydro-meteorological thresholds. Nat. Hazards Earth Syst. Sci. 18 (1), 31–39.
Burnash, R.J., Ferral, R.L., McGuire, R.A., 1973. A generalized streamflow simulation system: Conceptual modeling for digital computers. US Department of Commerce, National Weather Service, and State of California.
Caine, N., 1980. The rainfall intensity-duration control of shallow landslides and debris flows. Geografiska Annaler: Ser. A, Phys. Geogr. 62 (1-2), 23–27.
Cao, Q., Qi, Y., 2014. The variability of vertical structure of precipitation in Huaihe River Basin of China: Implications from long-term spaceborne observations with TRMM precipitation radar. Water Resour. Res. 50 (5), 3690–3705.
Chao, L., Zhang, K., Li, Z., Zhu, Y., Wang, J., Yu, Z., 2018. Geographically weighted regression based methods for merging satellite and gauge precipitation. J. Hydrol. 558, 275–289.
Cheema, M.J.M., Bastiaanssen, W.G.M., 2012. Local calibration of remotely sensed rainfall from the TRMM satellite for different periods and spatial scales in the Indus Basin. Int. J. Remote Sens. 33 (8), 2603–2627.
Chen, H., Chandrasekar, V., Tan, H., Cifelli, R., 2019. Rainfall Estimation From Ground Radar and TRMM Precipitation Radar Using Hybrid Deep Neural Networks. Geophys. Res. Lett. 46 (17-18), 10669–10678.
Chen, J., Zeng, Z., Jiang, P., Tang, H., 2015. Deformation prediction of landslide based on functional network. Neurocomputing 149, 151–157.
Crawford, N.H. and Linsley, R.K., 1966. Digital Simulation in Hydrology'Stanford Watershed Model 4.
Chen, X., Zhang, K., Chao, L., Liu, Z., Du, Y., Xu, Q., 2021. Quantifying natural recharge characteristics of shallow aquifers in groundwater overexploitation zone of North China. Water Sci. Eng. 14 https://doi.org/10.1016/j.wse.2021.07.001.
Duan, J., Miller, N.L., 1997. A generalized power function for the subsurface transmissivity profile in TOPMODEL. Water Resour. Res. 33 (11), 2559–2562.
Fawcett, T., 2006. An introduction to ROC analysis. Pattern Recogn. Lett. 27 (8), 861–874.
Fookes, P.G., 1997. Geology for engineers: the geological model, prediction and performance. Q. J. Eng. Geol. Hydrogeol. 30 (4), 293–424.
Gadelha, A.N., Coelho, V.H.R., Xavier, A.C., Barbosa, L.R., Melo, D.C.D., Xuan, Y., Huffman, G.J., Petersen, W.A., Almeida, C.D.N., 2019. Grid box-level evaluation of IMERG over Brazil at various space and time scales. Atmos. Res. 218, 231–244.
Glade, T., Crozier, M., Smith, P., 2000. Applying probability determination to refine landslide-triggering rainfall thresholds using an empirical "Antecedent Daily Rainfall Model". Pure Appl. Geophys. 157 (6–8), 1059–1079.
Griffith, C.G., Woodley, W.L., Grube, P.G., Martin, D.W., Stout, J., Sikdar, D.N., 1978. Rain estimation from geosynchronous satellite imagery—Visible and infrared studies. Mon. Weather Rev. 106 (8), 1153–1171.
Griffiths, J.S., 2002. Mapping in engineering geology. Geological Society of London.
Griffiths, J.S., Edwards, R.J.G., 2001. The development of land surface evaluation for engineering practice. Geol. Soc. London Eng. Geol. Spec. Publ. 18 (1), 3–9.
Guha-Sapir, D., Hargitt, D., Hoyois, P., 2004. Thirty years of natural disasters 1974–2003: The numbers. Presses univ, de Louvain.
Guzzetti, F., Cardinali, M., Reichenbach, P., Carrara, A., 2000. Comparing Landslide Maps: A Case Study in the Upper Tiber River Basin. Central Italy. Environ. Manage. 25 (3), 247–263.
Guzzetti, F., Peruccacci, S., Rossi, M., Stark, C.P., 2007. Rainfall thresholds for the initiation of landslides in central and southern Europe. Meteorol. Atmos. Phys. 98 (3-4), 239–267.
Guzzetti, F., Peruccacci, S., Rossi, M., Stark, C.P., 2008. The rainfall intensity–duration control of shallow landslides and debris flows: an update. Landslides 5 (1), 3–17.
He, X., Hong, Y., Vergara, H., Zhang, K., Kirstetter, P.-E., Gourley, J.J., Zhang, Y.u., Qiao, G., Liu, C., 2016. Development of a coupled hydrological-geotechnical framework for rainfall-induced landslides prediction. J. Hydrol. 543, 395–405.
He, B., Huang, X., Ma, M., Chang, Q., Tu, Y., Li, Q., Zhang, K., Hong, Y., 2018. Analysis of flash flood disaster characteristics in China from 2011 to 2015. Nat. Hazards 90 (1), 407–429. https://doi.org/10.1007/s11069-017-305207.
Hong, H., et al., 2017. Rainfall-induced landslide susceptibility assessment at the Chongren area (China) using frequency ratio, certainty factor, and index of entropy. Geocarto Int. 32 (2), 139–154.
Hong, H., Pradhan, B., Xu, C., Tien Bui, D., 2015. Spatial prediction of landslide hazard at the Yihuang area (China) using two-class kernel logistic regression, alternating decision tree and support vector machines. Catena 133, 266–281.
Hong, Y., Hsu, K.L., Sorooshian, S., Gao, X.G., 2005. Improved representation of diurnal variability of rainfall retrieved from the Tropical Rainfall Measurement Mission Microwave Imager adjusted Precipitation Estimation From Remotely Sensed Information Using Artificial Neural Networks (PERSIANN) system. J. Geophys. Res. D06102.
Hsu, K.-L., Gao, X., Sorooshian, S., Gupta, H.V., 1997. Precipitation estimation from remotely sensed information using artificial neural networks. J. Appl. Meteorol. 36 (9), 1176–1190.
Huang, X., Li, Z., Yu, D., Xu, Q., Fan, J., Hao, Z., Niu, Y., 2017. Evolution of a giant debris flow in the transitional mountainous region between the Tibetan Plateau and the Qinling Mountain range, Western China: Constraints from broadband seismic records. J. Asian Earth Sci. 148, 181–191.
Huffman, G.J. et al., 2019. Algorithm Theoretical Basis Document (ATBD) Version 5.1: NASA Global Precipitation Measurement (GPM) Integrated Multi-satellitE Retrievals for GPM (IMERG), NASA/GSFC, Greenbelt, MD, USA.
Hughes, D.A., 2006. Comparison of satellite rainfall data with observations from gauging station networks. J. Hydrol. 327 (3-4), 399–410.
Jonkman, S.N., 2005. Global perspectives on loss of human life caused by floods. Nat. Hazards 34 (2), 151–175.
Joyce, R.J., Janowiak, J.E., Arkin, P.A., Xie, P., 2004. CMORPH: A method that produces global precipitation estimates from passive microwave and infrared data at high spatial and temporal resolution. J. Hydrometeorol. 5 (3), 487–503.
Krajewski, W.F., Smith, J.A., 2002. Radar hydrology: rainfall estimation. Adv. Water Resour. 25 (8-12), 1387–1394.
Krige, D.G., 1951. A statistical approach to some mine valuation and allied problems on the Witwatersrand: By DG Krige. University of the Witwatersrand.
Kummerow, C., Barnes, W., Kozu, T., Shiue, J., Simpson, J., 1998. The tropical rainfall measuring mission (TRMM) sensor package. J. Atmos. Oceanic Technol. 15 (3), 809–817.
Le, X.-H., Lee, G., Jung, K., An, H.-u., Lee, S., Jung, Y., 2020. Application of Convolutional Neural Network for Spatiotemporal Bias Correction of Daily Satellite-Based Precipitation. Remote Sens. 12 (17), 2731. https://doi.org/10.3390/rs12172731.
Liao, Z., Hong, Y., Wang, J., Fukuoka, H., Sassa, K., Karnawati, D., Fathani, F., 2010. Prototyping an experimental early warning system for rainfall-induced landslides in Indonesia using satellite remote sensing and geospatial datasets. Landslides 7 (3), 317–324.
Ma, Y., Hong, Y., Chen, Y., Yang, Y., Tang, G., Yao, Y., Long, D., Li, C., Han, Z., Liu, R., 2018a. Performance of optimally merged multisatellite precipitation products using the dynamic Bayesian model averaging scheme over the Tibetan Plateau. J. Geophys. Res.: Atmos. 123 (2), 814–834.
Ma, Y., Yang, Y., Han, Z., Tang, G., Maguire, L., Chu, Z., Hong, Y., 2018b. Comprehensive evaluation of ensemble multi-satellite precipitation dataset using the dynamic bayesian model averaging scheme over the Tibetan Plateau. J. Hydrol. 556, 634–644.
Montrasio, L., Valentino, R., 2008. A model for triggering mechanisms of shallow landslides. Nat. Hazards Earth Syst. Sci. 8 (5), 1149–1159.
Montrasio, L., Valentino, R., 2016a. Modelling rainfall-induced shallow landslides at different scales using SLIP-Part I. Procedia Engineer 158, 476–481.
Montrasio, L., Valentino, R., 2016b. Modelling rainfall-induced shallow landslides at different scales using SLIP-Part II. Procedia Eng. 158, 482–486.
Peruccacci, S., Brunetti, M.T., Luciani, S., Vennari, C., Guzzetti, F., 2012. Lithological and seasonal control on rainfall thresholds for the possible initiation of landslides in central Italy. Geomorphology 139-140, 79–90.

Petley, D.N., 2010. On the impact of climate change and population growth on the occurrence of fatal landslides in South, East and SE Asia. Q. J. Eng. Geol. Hydrogeol. 43 (4), 487–496.
Pradhan, B., Youssef, A.M., 2010. Manifestation of remote sensing data and GIS on landslide hazard analysis using spatial-based statistical models. Arabian J. Geosci. 3 (3), 319–326.
Qi, Y., Zhang, J., 2013. Correction of radar QPE errors associated with low and partially observed brightband layers. J. Hydrometeorol. 14 (6), 1933–1943.
Qi, Y., Zhang, J., Cao, Q., Hong, Y., Hu, X.-M., 2013a. Correction of radar QPE errors for nonuniform VPRs in mesoscale convective systems using TRMM observations. J. Hydrometeorol. 14 (5), 1672–1682.
Qi, Y., Zhang, J., Zhang, P., 2013b. A real-time automated convective and stratiform precipitation segregation algorithm in native radar coordinates. Q. J. R. Meteorolog. Soc. 139 (677), 2233–2240.
Qi, Y., Zhang, J., Zhang, P., Cao, Q., 2013c. VPR correction of bright band effects in radar QPEs using polarimetric radar observations. J. Geophys. Res. : Atmos. 118 (9), 3627–3633.
Renard, B., Kavetski, D., Kuczera, G., Thyer, M., Franks, S.W., 2010. Understanding predictive uncertainty in hydrologic modeling: The challenge of identifying input and structural errors. Water Resour. Res. 46 (5) https://doi.org/10.1029/2009WR008328.
Seo, B.-C., Krajewski, W.F., Qi, Y., 2020. Utility of Vertically Integrated Liquid Water Content for Radar-Rainfall Estimation: Quality Control and Precipitation Type Classification. Atmos. Res. 236, 104800. https://doi.org/10.1016/j.atmosres.2019.104800.
Shen, X., Hong, Y., Zhang, K., Hao, Z., 2017. Refining a distributed linear reservoir routing method to improve performance of the CREST model. J. Hydrol. Eng. 22 (3), 04016061. https://doi.org/10.1061/(ASCE)HE.1943-5584.0001442.
Shen, Y., Xiong, A., Wang, Y., Xie, P., 2010. Performance of high-resolution satellite precipitation products over China. J. Geophys. Res.: Atmos. 115 (D2) https://doi.org/10.1029/2009JD012097.
Sivasubramaniam, K., Sharma, A., Alfredsen, K., 2019. Merging radar and gauge information within a dynamical model combination framework for precipitation estimation in cold climates. Environ. Modell. Software 119, 99–110.
Smith, J.A., Krajewski, W.F., 1991. Estimation of the mean field bias of radar rainfall estimates. J. Appl. Meteorol. 30 (4), 397–412.
Sugawara, M., Watanabe, I., Ozaki, E. and Katsugama, Y., 1984. Tank model with snow component. Research Notes of the National Research Center for Disaster Prevention No. 65. Science and Technolgoy, Ibaraki-Ken, Japan.
Tang, G., Behrangi, A., Long, D.i., Li, C., Hong, Y., 2018. Accounting for spatiotemporal errors of gauges: A critical step to evaluate gridded precipitation products. J. Hydrol. 559, 294–306.
Tavakol-Davani, H., Nasseri, M., Zahraie, B., 2013. Improved statistical downscaling of daily precipitation using SDSM platform and data-mining methods. Int. J. Climatol. 33 (11), 2561–2578.
Ushio, T. et al., 2003. The global satellite mapping of precipitation (GSMaP) project. Aqua (AMSR-E), 2004.
van Asch, T.W.J., Van Beek, L.P.H., Bogaard, T.A., 2007. Problems in predicting the mobility of slow-moving landslides. Eng. Geol. 91 (1), 46–55.
Wang, J., Hong, Y., Li, L.i., Gourley, J.J., Khan, S.I., Yilmaz, K.K., Adler, R.F., Policelli, F. S., Habib, S., Irwn, D., Limaye, A.S., Korme, T., Okello, L., 2011. The coupled routing and excess storage (CREST) distributed hydrological model. Hydrol. Sci. J. 56 (1), 84–98.
Wang, S., Zhang, K., van Beek, L.P.H., Tian, X., Bogaard, T.A., 2020. Physically-based landslide prediction over a large region: Scaling low-resolution hydrological model results for high-resolution slope stability assessment. Environ. Modell. Software 124, 104607. https://doi.org/10.1016/j.envsoft.2019.104607.
Wilkinson, P.L., Anderson, M.G., Lloyd, D.M., Renaud, J.-P., 2002. Landslide hazard and bioengineering: towards providing improved decision support through integrated numerical model development. Environ. Modell. Software 17 (4), 333–344.
Wilson, J.W., Brandes, E.A., 1979. Radar measurement of rainfall—A summary. Bull. Am. Meteorol. Soc. 60 (9), 1048–1058.
Wu, L.u., Zhai, P., 2012. Validation of daily precipitation from two high-resolution satellite precipitation datasets over the Tibetan Plateau and the regions to its east. Acta Meteorol. Sinica 26 (6), 735–745.
Xue, X., Hong, Y., Limaye, A.S., Gourley, J.J., Huffman, G.J., Khan, S.I., Dorji, C., Chen, S., 2013. Statistical and hydrological evaluation of TRMM-based Multi-satellite Precipitation Analysis over the Wangchu Basin of Bhutan: Are the latest satellite precipitation products 3B42V7 ready for use in ungauged basins? J. Hydrol. 499, 91–99.
Xue, X., Zhang, K., Hong, Y., Gourley, J.J., Kellogg, W., McPherson, R.A., Wan, Z., Austin, B.N., 2016. New Multisite Cascading Calibration Approach for Hydrological Models: Case Study in the Red River Basin Using the VIC Model. J. Hydrol. Eng. 21 (2), 05015019. https://doi.org/10.1061/(ASCE)HE.1943-5584.0001282.
Zhang, K., Niu, J., Li, X., Chao, L., 2021. Comparison of artificial intelligence flood forecasting models in China's semi-arid and semi-humid regions. Water Resour. Prot. 37 (1), 28–35+60. https://doi.org/10.3880/j.issn.1004-6933.2021.01.005.
Zhang, J., Qi, Y., 2010. A real-time algorithm for the correction of brightband effects in radar-derived QPE. J. Hydrometeorol. 11 (5), 1157–1171.
Zhang, K.e., Wang, S., Bao, H., Zhao, X., 2019a. Characteristics and influencing factors of rainfall-induced landslide and debris flow hazards in Shaanxi Province, China. Nat. Hazards Earth Syst. Sci. 19 (1), 93–105.
Zhang, K., Wang, S., Bao, H.J., Zhao, X.M., 2019b. Characteristics and influencing factors of rainfall-induced landslide and debris flow hazards in Shaanxi Province. China. Nat Hazard Earth Sys 19 (1), 93–105.
Zhang, K., Wu, N., Xu, G., Liu, L., Fan, Y., Zhang, Q., Zhou, J., Liu, T., 2021. An extraction method for contiunous water body through cloud interference removal using GF-1 remote sensing and DEM. J. Hohai Univ. 49 (4), 295–302.
Zhang, K., Xue, X., Hong, Y., Gourley, J.J., Lu, N., Wan, Z., Hong, Z., Wooten, R., 2016. iCRESTRIGRS: a coupled modeling system for cascading flood–landslide disaster forecasting. Hydrol. Earth Syst. Sci. 20 (12), 5035–5048.
Zhu, Z., Qi, Y., Cao, Q., Li, D., Zhang, Z., 2020. Conversion of the Vertical Profile of Reflectivity From Ku-Band to C-Band Based on the Drop Size Distribution Measurements of the Global Precipitation Measurement Mission Dual-Frequency Precipitation Radar. IEEE Trans. Geosci. Remote Sens. 59 (7), 5630–5641.
Zhu, Z., et al., 2020b. Particle Size Distribution Characteristics Within Different Regions of Mature Squall-Line Based on the Analysis of Global Precipitation Measurement Dual-Frequency Precipitation Radar Retrieval. IEEE Geosci. Remote Sens. Lett.